1 **Supplementary Materials**

2 # Electromagnetic interference shield of highly
3 # thermal-conducting, light-weight, and flexible
4 # electrospun nylon 66 nanofiber-silver multi-layer
5 # film

6 **Jaeyeon Kim** [1,†]**, Suyeong Lee** [1,†]**, Changho Kim** [1,†]**, Yeongcheol Park** [1]**, Mi-Hyun Kim** [2]**, and Jae**
7 **Hun Seol** [1,*]

8 [1]  School of Mechanical Engineering, Gwangju Institute of Science and Technology (GIST), Buk-gu, Gwangju
9     61005, Korea; bestkjy0426@gmail.com (J.K.); silver4fox@gm.gist.ac.kr (S.L.); umtoss530@gist.ac.kr (C.K.);
10     young13id@gist.ac.kr (Y.P.);
11 [2]  ICT Materials & Components Research Laboratory, ETRI, 218 Gajeong-ro, Yuseong-gu, Daejeon 305-700,
12     Korea; kmhyun@etri.re.kr (M.-H.K);
13
14 *  Correspondence: jhseol@gist.ac.kr
15 †  These authors contributed equally to this work.

16 **Morphology of the fabricated samples: E-0, N-0, E-50, and N-50**

17     Figure S1 shows plan-view SEM images of the fabricated samples as listed in Table 1 in the
18 Manuscript. The samples, which consist of only nylon 66 without Ag layers, *i.e.*, E-0 and N-0, are
19 shown in Fig. S1(a) and (b). Also, SEM images of the Ag layers in E-50 and N-50 are presented in Fig.
20 3(d) in the Manuscript and Fig. S1(c), respectively. Although the Ag layer in E-50 was annealed and
21 flattened after hot-pressing, the porous and anisotropic structure of the nylon 66 mat was still
22 preserved as shown in Fig. 3(d). In addition, the non-porous structure of the nylon 66 film remained
23 intact after the Ag deposition and subsequent hot-pressing process as shown in Fig. S1(c). However,
24 there were some imperfections such as pores and non-uniform thickness.
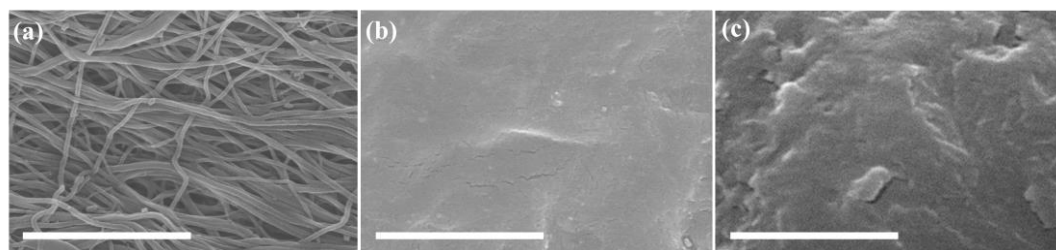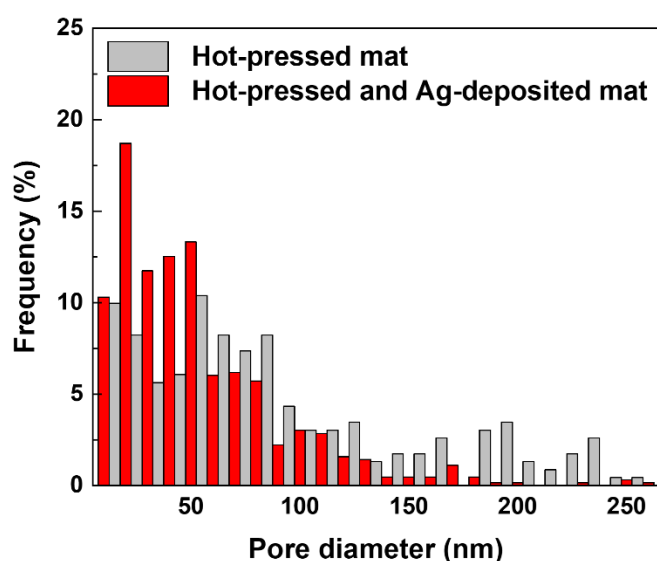


26 **Figure S1.** SEM images of the nylon 66 and/or the deposited Ag layers in (a) E-0, (b) N-0, and (c) N-
27 50. The scale bars are 2 μm.

29 **Pore size distributions of ethanol-treated and hot-pressed mats with and without the Ag-**
30 **deposition**



31

32 **Figure S2.** Pore size distributions of the ethanol-treated and then hot-pressed mats without (gray) and
33 with (red) the Ag-deposition. The average pore diameter of the former and latter is 100.0 and 58.6 nm,
34 respectively. The portion of pores with smaller size increases during the metal deposition process.

35 **DSC analysis**

36 To characterize the effect of the hot-pressing temperature on the crystallization of nylon 66
37 electrospun mats, DSC measurements were conducted while ramping temperatures from 40 to 300
38 °C at a heating rate of 10 °C/min and using a nitrogen purge gas. Figure S3(a) shows the DSC
39 thermographs of the electrospun mats, which were hot-pressed under different temperatures. During
40 the heating runs, broad endotherm peaks were observed at low temperatures because of solvent
41 evaporation[1]. Table S1 shows the analysis results of the DSC measurements, which summarize the
42 two endothermic temperatures, melting enthalpy, and crystallinity of the electrospun mats. The
43 electrospun mats have two melting endotherms without cold crystallization, which indicates that
44 those melting endotherms originate from imperfect $\alpha$-phase formed during the electrospinning
45 process [1]. In addition, one of the endotherm peaks disappeared after hot-pressing above 120 °C.
46 The crystallinity was calculated based on the ratio of melting enthalpy $(\Delta H_m)$ to that of theoretical
47 100% crystalline nylon 66 ($\Delta H_m^0 = 200.8$ J/g) [2]. Figure S3(b) shows the degree of crystallinity of the
48 mats and film in relation to the hot-pressing temperature. The crystallinity of mats gradually
49 increased with the hot-pressing temperature because polymeric molecules are better recrystallized at
50 higher annealing temperature [3,4]. Therefore, the mats hot-pressed at higher temperature have
51 higher crystallinity values. Moreover, the film was hot-pressed only at 160 °C, and it shows
52 crystallinity similar to the crystallinity of a mat hot-pressed at 70–120 °C.

53 **Table S1.** Two melting endotherms, melting enthalpy, and crystallinity of the DSC measurements

| Sample | $T_{m1}$ (°C) | $T_{m2}$ (°C) | $\Delta H_m$ (J/g) | Crystallinity (%) |
|---|---|---|---|---|
| **As-spun** | 260.56 | 269.74 | 80.22 | 38.9 |
| **Ethanol-treated** | 260.35 | 267.60 | 87.82 | 42.6 |
| **Ethanol-treated/hot-pressed at 40 °C** | 260.64 | 265.04 | 84.01 | 40.8 |
| **Ethanol-treated/hot-pressed at 70 °C** | 262.66 | 268.02 | 87.96 | 42.7 |
| **Ethanol-treated/hot-pressed at 120 °C** | | 267.06 | 88.45 | 42.9 |
| **Ethanol-treated/hot-pressed at 160 °C** | | 265.93 | 95.20 | 46.2 |

| Ethanol-treated/hot-pressed at 200 °C | 266.02 | 97.63 | 47.4 |
|---|---|---|---|

**(a)**

**(b)**
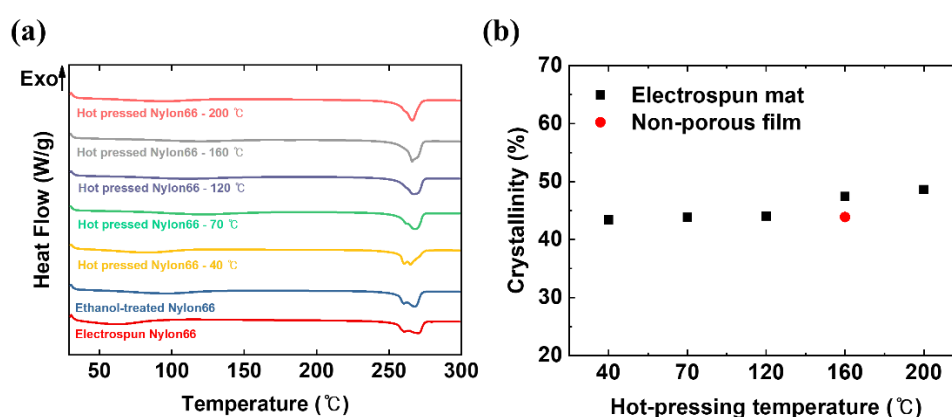


**Figure S3.** DSC measurement results of the electrospun nylon 66 mats and film. (a) DSC thermographs of the electrospun mats produced from as-spun, ethanol-treated, and ethanol-treated mats hot-pressed at 40, 70, 120, 160, and 200 °C. (b) Measured crystallinity using DSC for ethanol-treated hot-pressed electrospun mat (black square) and ethanol-treated hot-pressed non-porous film (red circle) as a function of the hot-pressing temperature. The crystallinity of non-porous film was hot-pressed only at 160 °C. The measurements were performed with a heating rate of 10 °C/min and a nitrogen purge gas.

## Contribution of electrical conductivity to SE$_A$

To investigate the relationship between the electrical conductivity and the absorption of the shield, electromagnetic interference shielding effectiveness (EMI SE) values, resulting from the different electrical conductivity of the deposited Ag layer in N-50 and E-50, were numerically calculated using COMSOL, as shown in Fig. S4. Because there exists a dependence of the absorption loss of an EM wave of a material on its electrical conductivity [5], the electrical conductivity of Ag is one of the factors which enhance the absorption during the multiple reflections. However, although the difference in electrical conductivity was considerable, as shown in Fig. 3 (Manuscript), the increase in absorption SE is insignificant. Therefore, the lower electrical conductivity of E-50 is also large enough to cause multiple reflections.
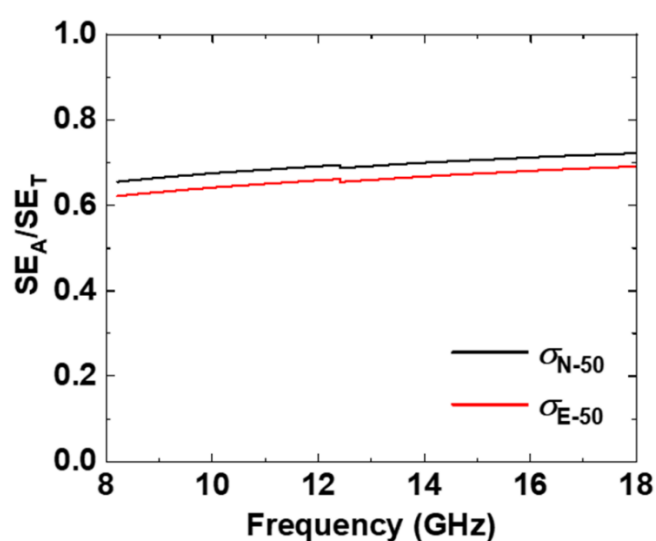


**Figure S4.** Numerically calculated SE$_A$/SE$_T$ of a multi-layered structure with applied electrical conductivity of Ag layers in N-50 (black continuous line) and E-50 (red continuous line) on the X- and K$_u$-bands.

76 Mesh configuration for numerical calculation



77
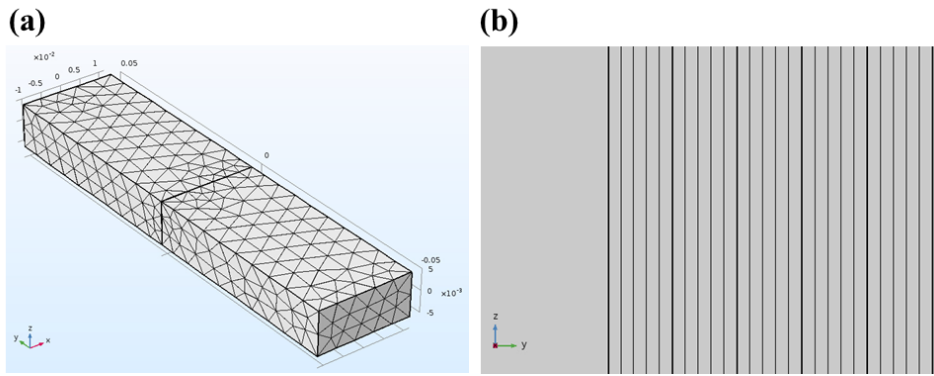
78 **Figure S5.** Mesh configurations for numerical calculation using COMSOL. (a) "Normal mesh" type
79 was applied as a waveguide, including a sample at the center of the waveguide. (b) Enlarged mesh
80 configuration in the central region of the waveguide.

81 **Analytical calculation of EMI SE**

82 The SE and the contribution of multiple inter-layer reflections of N-50 were analytically
83 calculated following the transfer-matrix method [6]. According to the transfer-matrix method, the
84 reflection coefficient and transmission coefficient of N-50 could be obtained using recursive
85 propagation matrices corresponding to each layer. The EM wave in a rectangular waveguide is a
86 plane wave and incident normally to the interface, and the electric field at position z can be described
87 as

$$E(z) = E_0^+ e^{-\gamma z} + E_0^- e^{\gamma z} = E^+(z) + E^-(z), \tag{S1}$$

88 where $E_0^+$ and $E_0^-$ are the arbitrary constant vectors that satisfy $\hat{z} \cdot E_0^\pm = 0$ and $\gamma$ is the
89 propagation constant, defined as $\gamma = \sqrt{j\omega\mu(\sigma + j\omega\varepsilon)}$ where $\mu, \sigma, \varepsilon$, and $\omega$ are the permeability,
90 conductivity, permittivity, and angular frequency of the incident EM wave, respectively. Figure S6(a)
91 shows a schematic cross-sectional view representing electric fields which propagate in the $i^{th}$ layer of
92 the multi-layer structure. Therefore, the electric field of the $i^{th}$ interface can be written as $E_i = E_i^+ +$
93 $E_i^-$, where $E_i^+$ and $E_i^-$ are the electric fields of $E_i$ propagating forward ($\hat{z}$) and backward ($-\hat{z}$),
94 respectively. Assuming homogenous and isotropic materials, the intrinsic impedance of the $i^{th}$ layer
95 is $\eta_i = \sqrt{j\omega\mu_i/(\sigma_i + j\omega\varepsilon_i)}$. Then, the reflection coefficient ($q_i$) and transmission coefficient ($p_i$) at the
96 $i^{th}$ interface are defined with the intrinsic impedance of $i^{th}$ and $(i-1)^{th}$ layers as follows:

$$E(z) = E_0^+ e^{-\gamma z} + E_0^- e^{\gamma z} = E^+(z) + E^-(z), \tag{S2}$$

$$E(z) = E_0^+ e^{-\gamma z} + E_0^- e^{\gamma z} = E^+(z) + E^-(z), \tag{S3}$$

97 From the transfer-matrix theory, the relation between $E_i^\pm$ and $E_{i+1}^\pm$ can be described as

$$\begin{pmatrix} E_i^+ \\ E_i^- \end{pmatrix} = M_i \begin{pmatrix} E_{i+1}^+ \\ E_{i+1}^- \end{pmatrix} = \frac{1}{p_i} \begin{pmatrix} e^{\gamma_i t_i} & q_i e^{\gamma_i t_i} \\ q_i e^{\gamma_i t_i} & e^{\gamma_i t_i} \end{pmatrix} \begin{pmatrix} E_{i+1}^+ \\ E_{i+1}^- \end{pmatrix}, \tag{S4}$$

98 where $M_i$, $\gamma_i$, and $t_i$ are the transfer-matrix, the propagation constant, and the thickness of the $i^{th}$
99 layer. The structure of N-50 is composed of four Ag layers ($i = 2, 4, 6, 8$) and five nylon 66 layers ($i =$
100 1, 3, 5, 7, 9), placed between two semi-infinite media of air ($i = 0, 10$) as shown in Fig. S6(b). The total
101 transfer matrix of N-50 ($M_{N-50}$) was calculated by multiplying the transfer-matrices for each layer,

$$\begin{pmatrix} E_1^+ \\ E_1^- \end{pmatrix} = \prod_{i=1}^{9} M_i \begin{pmatrix} E_{10}^+ \\ E_{10}^- \end{pmatrix} = \prod_{i=1}^{9} M_i \frac{1}{p_{10}} \begin{pmatrix} E'^+_{10} \\ 0 \end{pmatrix} = M_{N-50} \begin{pmatrix} E'^+_{10} \\ 0 \end{pmatrix} \tag{S5}$$

$$M_{N-50} = \frac{1}{p_{10}} \prod_{i=1}^{9} M_i = \begin{pmatrix} a & b \\ c & d \end{pmatrix}, \tag{S6}$$

102 where $E'^+_{10}$ is the electric field transmitted through N-50 toward the air. Using the definition of a
103 scattering matrix, the S-parameters of N-50 can be calculated using the components of $M_{N-50}$ as

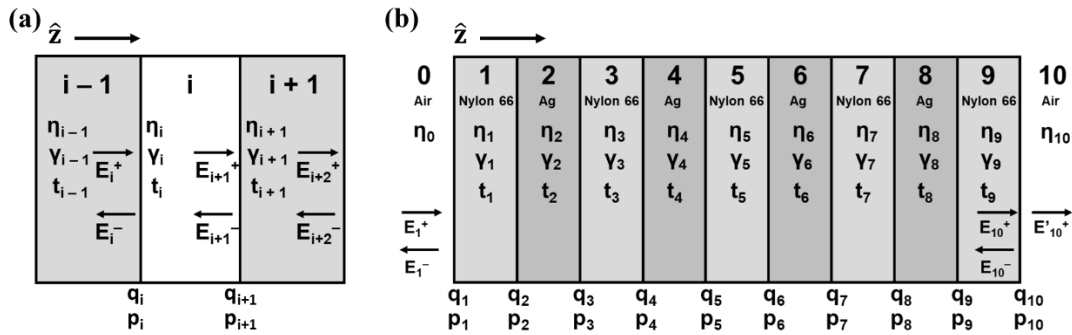$$S_{11} = \frac{E_1^-}{E_1^+} = \frac{c}{a} \tag{S7}$$

$$S_{21} = \frac{E'^+_{10}}{E_1^+} = \frac{1}{a} \tag{S8}$$

104 according to Eq. (1–3) in the Manuscript, the SE can be calculated from these results as follows:

$$SE_R = -10 \log(1 - \left|\frac{c}{a}\right|^2) \tag{S9}$$

$$SE_A = -10 \log(\left|\frac{1}{a}\right|^2 / (1 - \left|\frac{c}{a}\right|^2)) \tag{S10}$$

$$SE_T = SE_A + SE_R \tag{S11}$$



105

106 **Figure S6.** Schematic cross-sectional diagrams of $i^{th}$ layer in a multi-layer structure and N-50. (a) The
107 $i^{th}$ interface refers to the left interface of the $i^{th}$ layer, and the $E_i^+$ and $E_i^-$ are forward ($\hat{z}$) and backward
108 ($-\hat{z}$) electric fields on the left side of the $i^{th}$ interface. Moreover, $q_i$ and $p_i$ refer to the reflection
109 coefficient and transmission coefficient at the $i^{th}$ interface. (b) Cross-section schematics of N-50. The
110 intrinsic impedance, propagation constant, and thickness of the $i^{th}$ layer are expressed as $\eta_i$, $\gamma_i$, and $t_i$,
111 respectively, when $i$ is 0 to 10.

112 Using these processes, the SE of N-50 was calculated using the measured electrical conductivity
113 of Ag in N-50, other material properties of Ag and nylon 66 from the literature [7,8], and MATLAB
114 software. Additionally, the contribution of inter-layer multiple reflections to $SE_A$ was obtained by
115 subtracting the penetration loss when the EM wave passes through a material without reflection. The
116 penetration loss contributes to $SE_A$ by attenuating the EM waves when it passes through the material.
117 According to the shielding theory [9], the penetration loss is defined as

$$SE_{A,penetration} \ (dB) = 20 \log \left| e^{\sum_{i=1}^{9} \gamma_i t_i} \right| \tag{S12}$$

118

## Influence of hot-press process on the porosity of E-50

As for the porosity calculations, the porosity ($\phi$) was calculated from a true density ($\rho_{true}$) and the density including pores ($\rho$), *i.e.*, $\phi = (\rho_{true} - \rho)/\rho_{true}$, where $\rho$ is calculated from the ratio of its mass to the volume. Figure S7 shows the porosity values of the as-spun, the firstly hot-pressed mat, and E-50. The firstly hot-pressed mat and E-50 were made of three as-spun mats and five firstly hot-pressed mats through the first and second hot-pressing processes, respectively. The obtained porosity values of the as-spun mat, the firstly hot-pressed three mat, and E-50 were 74.3, 70.0, and 27.7%, respectively. The porosity decreased drastically by a factor of 2.5 after the second hot-pressing process. The thickness values of the feeler gauges, which were used for the first and second hot-pressing processes, were 30 and 100 μm, respectively. Although the thicker feeler gauge was used for the second hot-pressing process, the effect of hot-pressing was more significant because five firstly hot-pressed mats were hot-pressed together.
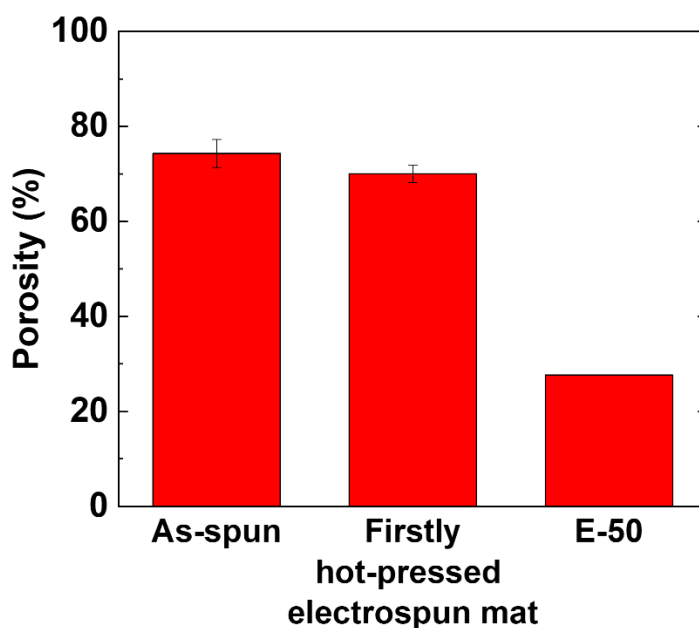


**Figure S7.** Porosity of as-spun, firstly hot-pressed electrospun mat, and E-50. Notably, the thickness of E-50 was enough to be measured, which made the error bar of E-50 unnoticeable.

## References

1.  Guerrini, L.M.; Branciforti, M.C.; Canova, T.; Bretas, R.E.S. Electrospinning and characterization of polyamide 66 nanofibers with different molecular weights. *Mater. Res.* **2009**, *12*, 181–190.
2.  Mark, J.E. *Physical properties of polymers handbook*; AIP Press: New york, NY, USA, 1996; ISBN 978-0-387-69002-5.
3.  Aly, A.A. Heat Treatment of Polymers: A Review. *Int. J. Mater. Chem. Phys.* **2015**, *1*, 132–140.
4.  Simal, O.; Martin, A.R. Structure of Heat-Treated Nylon 6 and 6.6 Fibers. I. The shrinkage mechanism. *J. Appl. Polym. Sci.* **1997**, *68*, 441–452.
5.  Kuruvilla, J.; Runcy, W.; Gejo, G. *Materials for Potential EMI Shielding Applications: Processing, Properties and Current Trends*; Elsevier Science, 2019; ISBN 9780128175910.
6.  Orfanidis, S.J.; Sophocles, J.O. Electromagnetic Waves and Antennas. *Media* **2003**, *2*, 313–321.
7.  Elmajid, H.; Terhzaz, J.; Ammor, H.; Chaibi, M.; Mediavilla Sánchez, Á. A new method to determine the complex permittivity and complex permeability of dielectric materials at X-band frequencies. *Int. J. Microw. Opt. Technol.* **2015**, *10*, 34–39.

148  8.  Wu, W.M.; Njoku, C.C.; Whittow, W.G.; Zagoskin, A.M.; Kusmartsev, F. V.; Vardaxoglou, J.C. Studies
149    of permittivity and permeability of dielectric matrix with cuboid metallic inclusions in different
150    orientations. *J. Adv. Dielectr.* **2014**, *04*, 1450032.
151  9.  Transactions, I.; Electromagnetic, O.N. Shielding theory and practice - Electromagnetic Compatibility,
152    IEEE Transactions on. **1988**, *30*, 187–201.
153